

15A.3 Onsite radome performance verification

Michael Frech,^{1*} Bertram Lange², Theo Mammen², Jörg Seltmann¹,
Chris Morehead³ and Joshua Rowan³

¹Deutscher Wetterdienst

Hohenpeissenberg Meteorological Observatory, Germany

²Deutscher Wetterdienst, Hamburg, Germany

³ EEC Enterprise Electronics Corporation, Enterprise, AL, USA

1. Introduction

The German Meteorological Service DWD is currently replacing all radar systems with new dualpolarization radars. With the introduction of dualpolarization systems improved quantitative precipitation estimations and a better classification of meteorological and non-meteorological targets are expected. This, however, requires good data quality delivered by the radar system. One of the key components is the antenna (e.g. Chandrasekar and Keeler, 1993, Zrnice et al., 2010, Bringi et al., 2011). In particular, the quality of dualpol moments is sensitive to the quality of the antenna and its proper characterization. Commonly the compliance with the specifications of the antenna is proven through antenna patterns which are usually provided by the antenna manufacturer as cuts through the main planes of the antenna including the strut plane. In the course of the acceptance tests of the antenna it appeared that for example the proof of the match between the main beam for both polarizations is limited with the existing equipment on the antenna manufacturer's test range. In particular the mechanical antenna pointing accuracy at the antenna manufacturer's site appeared not sufficient to show the compliance with our specifications. We therefore test the antennas on the radar manufacturer's test range making use of the capabilities of the new radar system. Those tests are carried out during factory acceptance tests (FAT) for

*Corresponding author address: Michael Frech, DWD, Meteorologisches Observatorium Hohenpeissenberg, D-82383 Hohenpeissenberg, Germany. Email: Michael.Frech@dwd.de
Extended abstract, AMS Radar conference 2011, Pittsburgh, PA.

the radar system delivered to DWD.

On site antenna tests are a unique effort during the radar replacement project. They have two main goals. One is to prove that the on site antenna assembly procedures guarantee the same antenna performance as shown during FAT. The second aspect is related to the combined performance of the antenna and the radome which in the end determine the operational data quality of the new dualpol radar system.

The radome is an important protecting component of the radar system as it guarantees a high availability of the radar system under bad weather conditions. On the other hand it must not affect the dualpol data quality in a significant way. For example, previous studies have shown azimuthal dependencies of differential moments due to the radome designs (e.g. Gourley et al., 2006). The specifications to the radome performance are strict and hard to prove. In an effort to prove parts of the radome performance, dedicated antenna pattern measurements with and without radome were carried out at the Hohenpeissenberg Meteorological Observatory in Spring 2011.

The radome that is installed together with the new radar system has a random panel design which is optimized for dualpol applications. The design is aiming at electrically seamless RF performance. The layout of the design is based on impedance matching procedures which include laboratory measurement of the electromagnetic field due to the scattering effect of the radome panels.

In the following we first give an overview about the an-

tenna and radome specifications. We then describe the approach to verify parts of the specifications. In the main body of this paper we discuss the results from the measurements before we summarize the main findings.

2. Brief description of the EEC radar DWSR5001C/SDP/CE

Here we summarize briefly some key aspects of the radar system relevant for this paper:

Pedestal unit: pointing accuracy $< 0.05^\circ$, maximum azimuth rate $48^\circ/\text{s}$

Receiver: The receiver is mounted behind the antenna (“receiver-over-elevation” concept). The analog signals are digitized by the ENIGMA3p IFD and the digitized IQ-data are transmitted in realtime through a fiber optic rotary joint to the ENIGMA3p signal processor which is mounted in the radar control cabinet.

Antenna: The parabolic antenna has a diameter of 4.3 m and consists of 9 elements. It is made of a composite material and has a center-fed antenna design with four struts supporting the dualpol feed.

Radome: The radome is manufactured by AFC and has a random panel design which is optimized for dualpol applications. The panels have a sandwich foam core design. They are coated with a highly hydrophobic material.

Signal processor: Linux based signalprocessor ENIGMA3p

3. Requirements to the antenna performance.

In dualpol application a good match of antenna characteristics of the two polarizations planes H and V is a prerequisite for a good performance of the radar system. In particular the mains beam in H and V require a good matching. Furthermore we are aiming at low side-lobe

levels in all planes including the struts. Low side levels are important in the presence of high spatial reflectivity gradients and low reflectivity situations where side lobe contributions may degrade data quality.

Following specifications for the new dualpol antenna where established:

- beam width (BW) $< 1^\circ$
- difference in H/V BW $< 0.03^\circ$
- beam squint $\leq 0.08^\circ$
- gain > 45 dB
- gain difference H/V ≤ 0.1 dB
- side lobe main axes < -30 dB ($< \pm 10^\circ$), < -43 dB ($> \pm 10^\circ$).
- cross-polar isolation < -32 dB
- axial symmetry < -5 dB in a range $< \pm 10^\circ$ around the main beam.

4. Requirements to the radome performance

Here we summarize the specifications of the radome:

- one way (dry) attenuation < 0.27 dB.
- beam squint caused by radome $< 0.02^\circ$.
- side lobe changes ≤ 0.5 dB
- variation of ZDR (in el and az) < 0.0005 dB.
- variation of Φ_{dp} (in az and el) $< 0.03^\circ$.
- one-way attenuation for ZH and ZV < 0.005 dB.
- variation of ρ_{hv} (in az and el) $< 0.005^\circ$ for $\rho_{hv} > 0.99$).
- variation of LDR (in az and el) < 1.5 dB.

These specifications indicate very high quality numbers as they were provided by the radome manufacturer. In principle, such small numbers will be difficult to prove in-field. In an attempt to quantify possible radome effects, we will analyze antenna patterns with and without the presence of a radome.

5. Hohenpeissenberg measurement set up and scan strategy

The basic approach to obtain an antenna pattern is to place a transmitter at the radar frequency in the far field of the receiving radar antenna. The location of the transmitter has to be chosen such that there are no obstacles in the path. Furthermore, the site has to be selected that minimum scattering at the orography along this path may occur. A favorable source site may be a tall tower or a mountain with e.g. a valley along the transmit path. Contrary to typical antenna test ranges, we have the new radar system with its precise positioning system and state-of-the-art radar receiver and signal processing available. This allows to acquire high resolution volume data during the pattern measurements. Figure 1 shows the radar system during one the pattern tests with and without radome. In total three external transmit sites could be identified for the Hohenpeissenberg test: Auerberg, Bromberg and the Hohenpeissenberg TV tower.

The Auerberg test site has been used in previous antenna pattern measurement campaigns. The Bromberg site is a new test site which has been chosen in order to evaluate Auerberg pattern with an independent set of measurements. In particular, it is expected that reflections due to obstacles in the vicinity of the radar site can be better identified. This then allows for a better quantitative interpretation of the antenna pattern. The third source site may further help in evaluating azimuthal dependencies in the RF field due to the radome. Some basic informations of the two sites are summarized in Table 1.

Dedicated antenna scans were defined using DWD's standard operational radar software MURAN 4.1 with following settings in STAR-mode:

1. "High" resolution volume with elevation angle steps of $\Delta el = 0.1^\circ$ close to the main beam and coarser elevation steps starting at 5° with $\Delta el = 0.5 - 1^\circ$ up to 30° elevation.
 - in general 117 sweeps are recorded starting from $el = -2^\circ$ to $el = 30^\circ$. Every 10 sweeps, one sweep is carried out at the elevation of maximum signal strength. This allows for a monitoring of the signal source during the scan.



Figure 1: Radar system during a pattern test in April 2011, upper picture without the radome, lower picture with the new radome.

Table 1: Basic information about the two transmitter sites, Auerberg and Bromberg, respectively.

| | Auerberg | Bromberg | TV tower |
|------------------------------|--------------------------|--------------------------|------------------------|
| Coordinates (lat/long) | 47°44'11"N 10°44'17"W | 47°43'38"N 11°01'53"W | 47°48'4"N 11°1'28"W |
| Height ASL | 1039 m | 952 m | 936 m z=158,76 m |
| Distance to radar site | 21.7 km | 8.5 km | 1.14 km |
| az/el Position rel. to radar | 250.25°/0.0° | 168.5°/-0.39° | 93.3°/+1.21° |

- $PRF = 3000$ Hz, AZ-rate $6^\circ/s$, range= 20 km.
- Raw-range bin resolution: 25 m, range averaging 1 km
- pulse width: $0.4 \mu s$
- Dynamic angle synching (DAS) with 0.05° ray width.
- The following moments are recorded: SNRh, SNRv, Φ_{dp} and UZDR.

2. RHI: in order to sample a larger range of the 90° plane, we carried out a number of RHI sweeps.

- in general 5 sweeps are recorded starting from $el = -2^\circ$ to $el = 90^\circ$.
- $PRF = 3000$ Hz, AZ-rate $6^\circ/s$, range= 20 km.
- Raw-range bin resolution: 25 m, range averaging 1 km
- pulse width: $0.4 \mu s$
- Dynamic angle synching (DAS) with 0.05° ray width.

The radar of course is not radiating during the scans, but peaked to the transmitting frequency. One volume scan and a set of usually four RHI scans for one polarization are acquired in about 2 1/2 hours.

The transmitter dish assembly is shown in Figure 2. The picture is taken at the Bromberg site. The dish has a diameter of 150 cm. A close-up view of the dual-pol feed is shown in Figure 3. On the TV-tower a different antenna assembly is used provided by EEC.

At the radar site, a standard gain horn provided an independent monitoring of the received power (Figure 4).

In total three transmit modes were used: H only, V only and V and H simultaneously. The latter is referred to as the STAR mode, where the source transmits linearly polarized signals in H and V at constant phase difference. In STAR mode we can measure antenna patterns of differential phase and power. When transmitting in single polarized mode (H or V only), the transmitted cross-polar signal is minimized manually by adjusting the feed before starting the volume scan. In general, a feed-dish assembly never shows a perfectly cross-isolation, so that the received cross-polar signal of the antenna pattern is at least in part related to the limited cross-isolation of the transmitting and antenna and feed.



Figure 2: The transmitter dish/feed assembly.



Figure 3: The single-pol feed of the transmitter dish.



Figure 4: Standard gain horn monitoring setup. The picture shows a view towards the Auerberg site.

6. Analysis of antenna patterns

a. The measurements

Fortunately, we had very stable and ideal weather conditions during SAT tests with and without radome. The measurement dates and the corresponding temperature ranges during the tests are summarized in Table 2. We document this for a proper interpretation of the antenna patterns.

b. Outline of the analysis

We focus on the difference between the measurements with and without radome. In order to obtain a more generalized view on the antenna performance and the radome we generate composites centered around the main lobe from all measurements and show average cuts through the main planes and their variability from measurement to measurement, and site to site. The best sampling is available for the zero degree plane where we have 20 sweeps for each polarization through the main beam for a particular source site. So in total 60 sweeps (three source sites) through the main plane are available for copolar measurements with and without radome each.

c. Antenna patterns with and without radome

We first show some examples of antenna patterns for a specific source site with and without radome in order to illustrate the main features of the radome influence on the antenna pattern.

The two examples show the copolar signal received from the TV tower site. Clearly visible are the pencil shaped main beam of the antenna and the struts. Figures 5 and 9 show copolar H signal without radome, and Figure 6 with radome. Qualitatively there is an increase in copolar signal in some locations to levels above -43 dB, but the difference between the two measurements seems not significant. Figures 7 and 8 show the corresponding cross-polar HV signal (transmit H, receive V). It is obvious, that the cross-polar levels are increased significantly by the radome structure. This increase is mainly seen in between the struts up to levels of about -50 dB. There seems to be no significant increase in the strut plane and the in the main beam region.

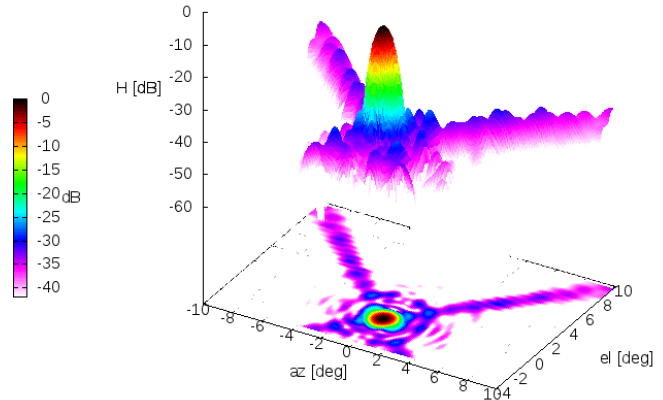


Figure 5: Copolar H plot, source site is the TV tower. Data are taken without radome.

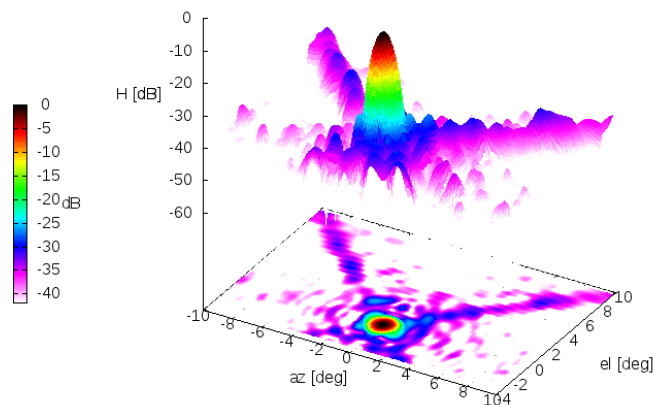


Figure 6: Copolar H plot, source site is the TV tower. Data are taken with radome.

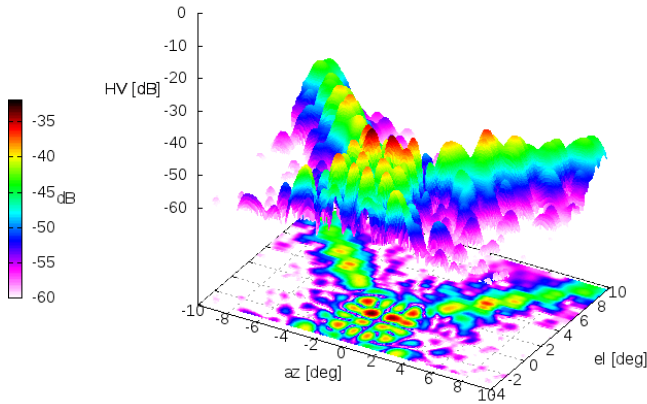


Figure 7: Copolar HV plot, source site is the TV tower. Data are taken without radome.

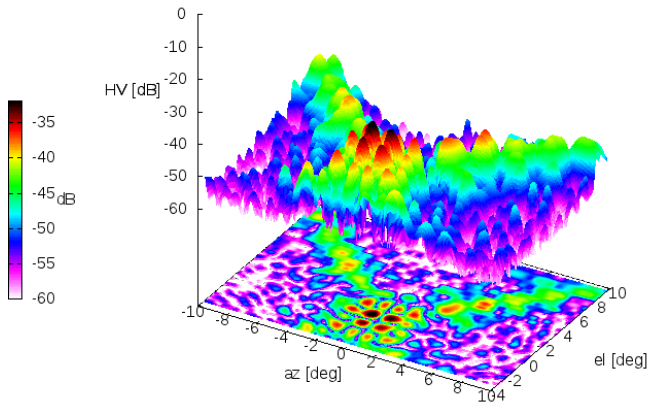


Figure 8: Copolar HV plot, source site is the TV tower. Data are taken with the radome in place.

Table 2: Temperature ranges during the antenna tests (in °C, time in UTC). Shown are source sites (AUER: Auerberg, BROM: Bromberg), the polarization during the test (H-V-STAR), date, duration, minimum, median and maximum temperature during the test.

| site / mode | Date / duration | Min | Med | Max |
|----------------|----------------------|------|------|------|
| without radome | | | | |
| BROM V | 5.4.11, 11:41-13:34 | 10.2 | 12.7 | 13.8 |
| BROM H | 5.4.11, 13:44-15:37 | 12.0 | 12.8 | 13.4 |
| BROM STAR | 5.4.11, 15:44-17:01 | 10.2 | 11.8 | 12.7 |
| AUER STAR | 6.4.11, 09:27-10:43 | 14.9 | 16.3 | 19.1 |
| AUER V | 6.4.11, 11:52-13:43 | 14.9 | 16.0 | 18.2 |
| AUER H | 6.4.11, 13:55-15:56 | 15.7 | 16.0 | 16.8 |
| TV V | 6.4.11, 16:15-18:07 | 13.1 | 15.1 | 16.7 |
| TV H | 6.4.11, 18:32-20:15 | 12.2 | 12.8 | 13.1 |
| TV STAR | 6.4.11, 20:48-22:10 | 11.9 | 12.2 | 12.6 |
| with radome | | | | |
| TV V | 11.4.11, 07:37-09:29 | 14.3 | 15.1 | 16.3 |
| TV H | 11.4.11, 09:35-11:27 | 16.3 | 17.3 | 18.5 |
| TV STAR | 11.4.11, 11:36-13:09 | 18.6 | 19.5 | 20.4 |
| BROM H | 21.4.11, 08:46-10:38 | 19.4 | 20.1 | 20.7 |
| BROM V | 21.4.11, 10:49-12:42 | 20.8 | 21.5 | 22.1 |
| BROM STAR | 21.4.11, 12:50-14:06 | 22.1 | 22.6 | 23.0 |
| AUER H | 18.5.11, 07:22-09:14 | 17.8 | 18.3 | 19.3 |
| AUER V | 18.5.11, 09:25-11:17 | 19.3 | 20.1 | 21.3 |
| AUER STAR | 18.5.11, 11:31-12:47 | 21.5 | 22.3 | 22.8 |

The typical four cross-polar peaks located around the center of the main beam are nicely visible (Figure 9, Zrnic et al., 2010).

As mentioned before, these figures provide a first qualitative view on the main features of the measured antenna patterns. In the following we will make a more quantitative analysis focusing on cuts through characteristic planes of the antenna diagram.

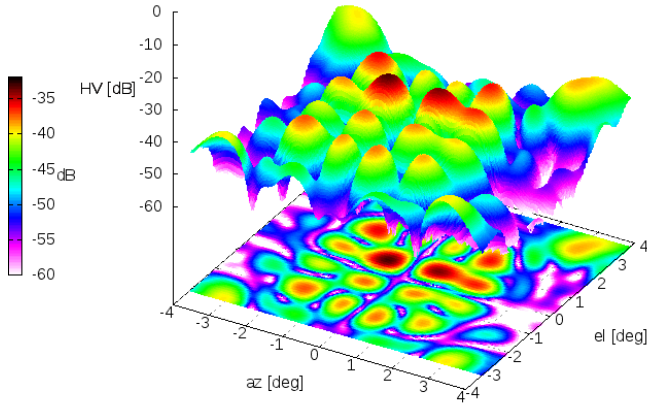


Figure 9: Cross-polar HV plot, source site is the TV tower. Data are taken without radome.

7. Slices through the main axes

Here we show slices through the main axis (0°), the 90° and the strut plane ($\pm 45^\circ$). We first show a comparison of the results from the three source sites without radome. Ideally, no differences should be expected. Any differences in the patterns from different source sites may be attributed to our test range conditions. In general, the results for the copolar measurements are similar from site to site. For example, the first side lobes match very well in location and level (Figure 10). Furthermore, the location of the side-lobes from the on site measurements match well with those from FAT. We note however, that the FAT side-lobe levels tend to differ from the on site measurements. We attribute this to the test range conditions during FAT. The cross-polar measurements show larger scatter (Figure 11). This can also be attributed to test range effects where part of the transmitted copolar signal may be scattered at obstacles along the propagation path. The state of the boundary layer may also contribute to scattering effects. We notice also an asymmetry in the first side lobe in H. The reason for this is not clear. This might be due to a lateral feed dis-alignment (Skolnik, 2008). The increased filling of the first null in the copolar H pattern compared to the V pattern may point

to different blocking effects due to the feed, depending on the polarization state.

In the following analysis, we average the measurements from on the different source sites as outlined before. This is done for the tests with and without radome and includes the measurements from the STAR tests where applicable. When averaging the data we also compute the 1st and 3rd quartile of the data which will serve as an indication of the antenna pattern variability as a function of azimuth angle. The resulting variability then can be attributed to the radome, test range effects and measurement uncertainties of the radar receiver. The variability due the radome may be attributed to the different azimuthal positions of source sites. As such the antenna aperture looks through different radome panel combination and geometries.

The average copolar results in H and V through the main plane (zero degree) show no significant differences between measurements with and without radome in the main beam area including the first side lobe (Figure 12, upper panel). There is a significant increase in side lobe levels beyond the first side lobes compared to the measurements without radome. The typical roll-off of the side lobes is not seen and the copolar signals remain on average on a constant level. At some azimuthal positions copolar levels are above the specified -43 dB level (Figure 12, lower panel). From an operational perspective, the levels of the first side lobes are important as they determine level of clutter echos at low elevations. Table 3 summarizes the average first side lobe levels in the main plane. Without radome, the antenna fails to achieve the specified maximum side lobe of -30 dB by 0.4 dB. The other side lobe levels are well within the specifications, also with the radome present. Based on the specification, the first side lobe must not be increased by > 0.5 dB due to the radome. Here in all but one case, this is achieved. In V, we find an increase of 0.9 dB (from -34.3 to -33.4 dB). This might be a measurement artifact, but the large number of measurements and the small variability from measurement to measurement suggest an effect related to the radome. However, the overall performance of the antenna-radome assembly with respect to the influence on the copolar antenna pattern in the main beam area is still very good. The corresponding cross-polar slices are shown in Figure 13. In the main beam there is no significant difference between measurements

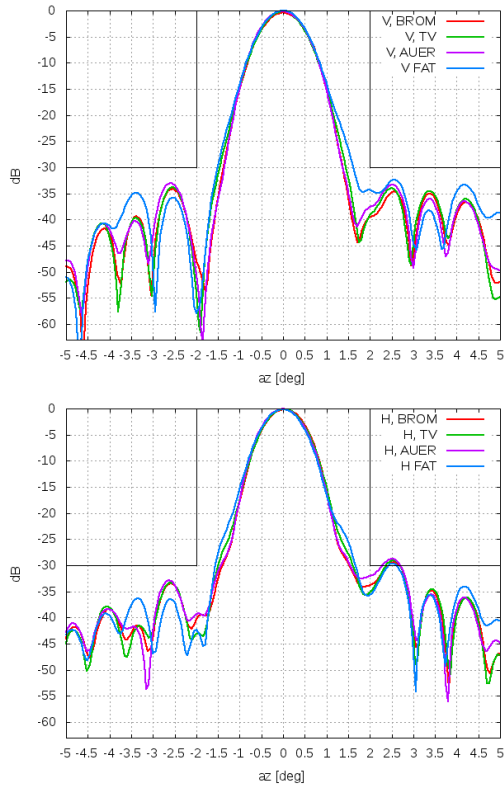


Figure 10: Slices through the 2-D pattern. Shown are copolar results through the main axes at 0° from measurements during FAT and SAT. We compare results from FAT at EEC, MOHP Bromberg (BROM), Auerberg (AUER) and the TV tower source site with a focus on the main beam area. The black graphs denote the specification.

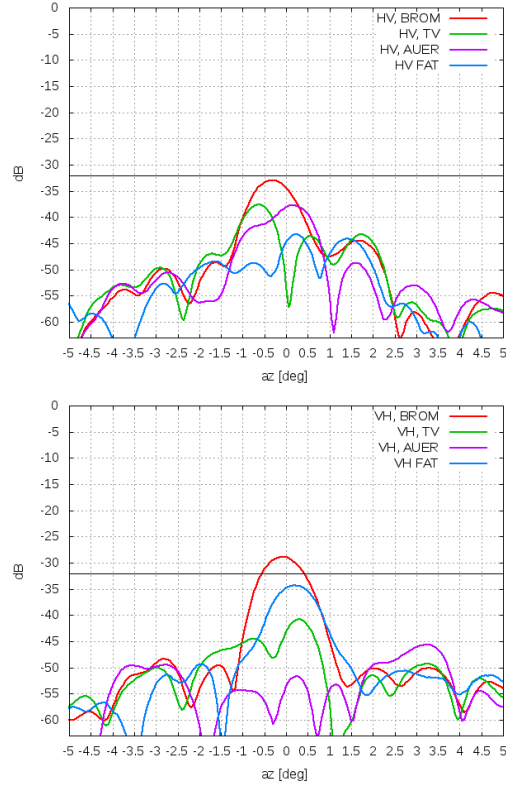


Figure 11: Slices through the 2-D pattern. Shown are cross-polar results through the main axes at 0° from measurements during FAT and SAT. We compare results from FAT at EEC, MOHP Bromberg (BROM), Auerberg (AUER) and the MOHP TV tower source site with a focus on the main beam area. The black graphs denote the specification.

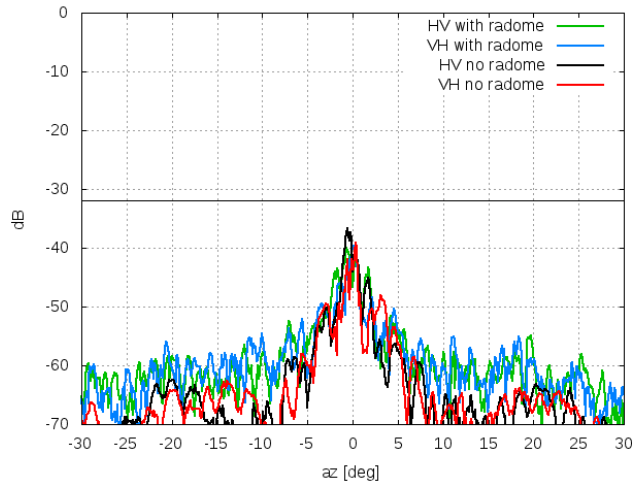
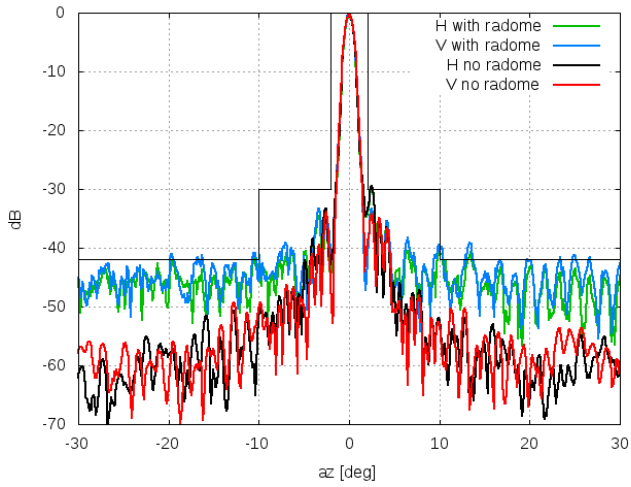
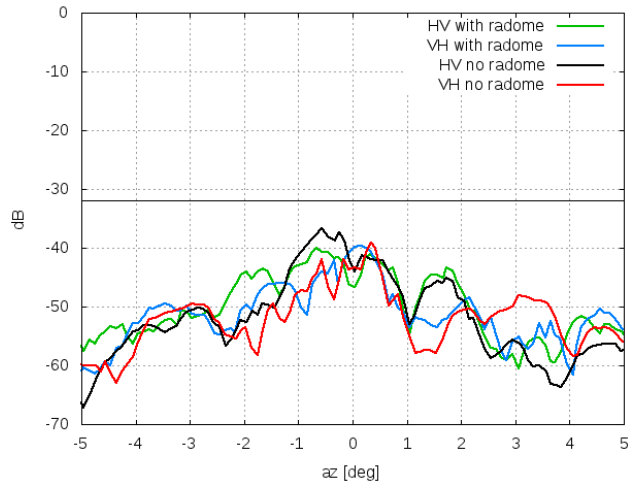
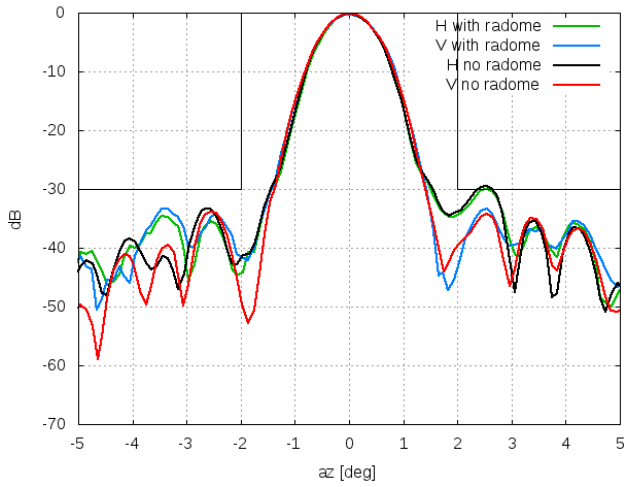


Figure 12: Average copolar power H and V, with and without radome. The average is based on 60 sweeps (single pol and STAR mode tests). Shown are also the antenna specifications.

Figure 13: Average cross-polar power HV (transmit H, receive V) and VH (transmit V, receive H), with and without radome. The average is based on 40 sweeps (single pol tests). Shown are also the antenna specifications.

Table 3: The average first side lobe levels in H and V for the measurements with and without radome. Power levels are relative to the main beam.

| polarization | w/o radome, az / power level | with radome, az / power level |
|--------------|---------------------------------|----------------------------------|
| H | -2.6° / -33.3 dB | -2.5° / -35.4 dB |
| | 2.5° / -29.6 dB | 2.5° / -30.0 dB |
| V | -2.5° / -33.8 dB | -2.4° / -34.3 dB |
| | 2.4° / -34.3 dB | 2.5° / -33.4 dB |

with and without radome. The cross-polar signal are about 10 dB larger for azimuth angles $> \pm 10^\circ$. However, on average the cross-polar levels are always within the specifications.

The variability (defined by the 1st and 3rd quartiles) of the copolar measurements with and without radome is shown in Figures 14 and 16. Largest variations are usually seen near minima where slight differences in azimuthal position can cause large variations. For data without radome, side lobe peaks usually show small variations which suggest quasi-constant azimuthal locations of those peaks between measurements. Those variations are larger for the measurements with radome. Though we have only three source sites with respectively different azimuthal positions, we might argue that the increased variability seen here can be attributed to the radome. In doing so, we relate this to an azimuthal dependence of the antenna pattern caused by the radome. This may be explained by different panel combinations seen by the antenna aperture at varying azimuthal positions and associated variable scattering effects.

The variability of the cross-polar measurements is shown in Figures 15 and 17. In the main beam area the observed variability is likely to be dominated by test range effects. Outside the main beam area we observe a similar behavior as for the copolar measurements: the variability of the cross-polar measurements is on average larger for measurements with radome.

Similar to the results for the main plane we now show the copolar side lobe levels in the strut plane ($\pm 45^\circ$). The mean copolar levels in the strut plane is based on an average over all three source sites (Figure 18). The number of samples for this average is much smaller than for

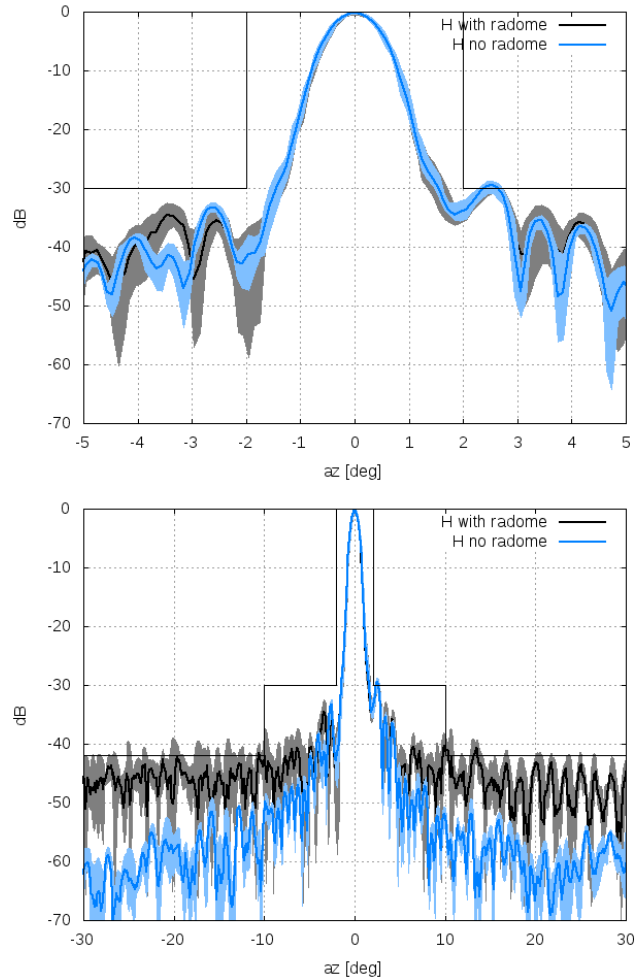


Figure 14: Variability of copolar power H with and without radome in the main plane. Shown are also the antenna specifications.

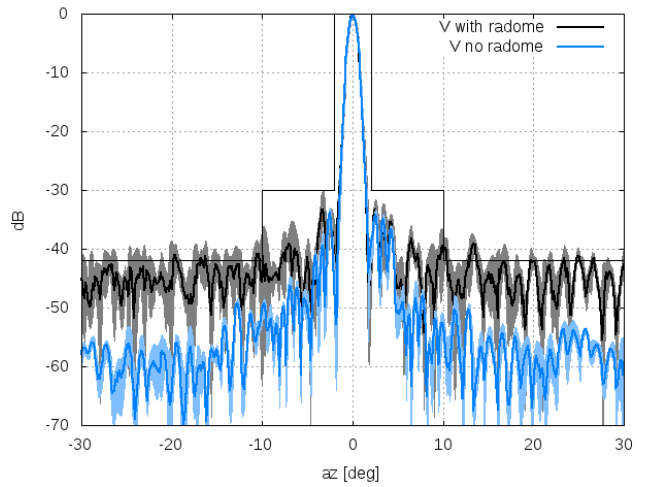
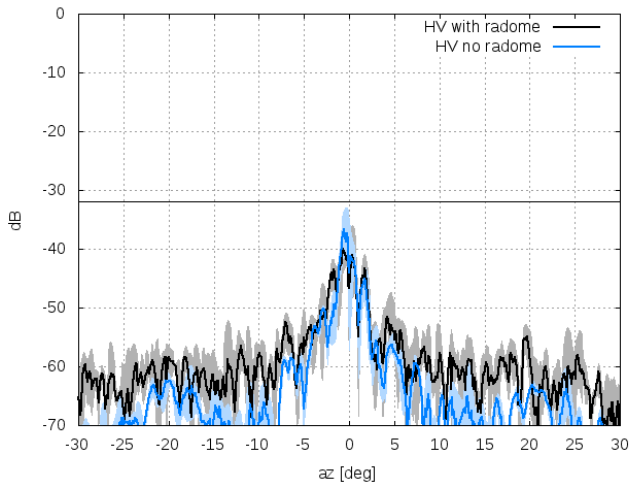
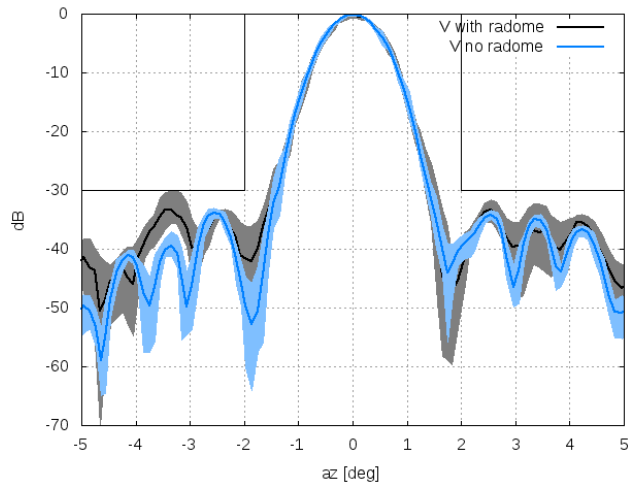
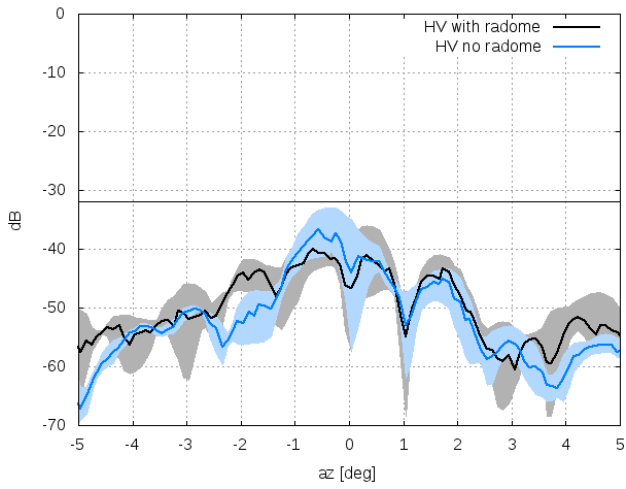


Figure 15: Variability of cross-polar power HV with and without radome in the main plane. Shown are also the antenna specifications.

Figure 16: Variability of copolar power V with and without radome in the main plane. Shown are also the antenna specifications.

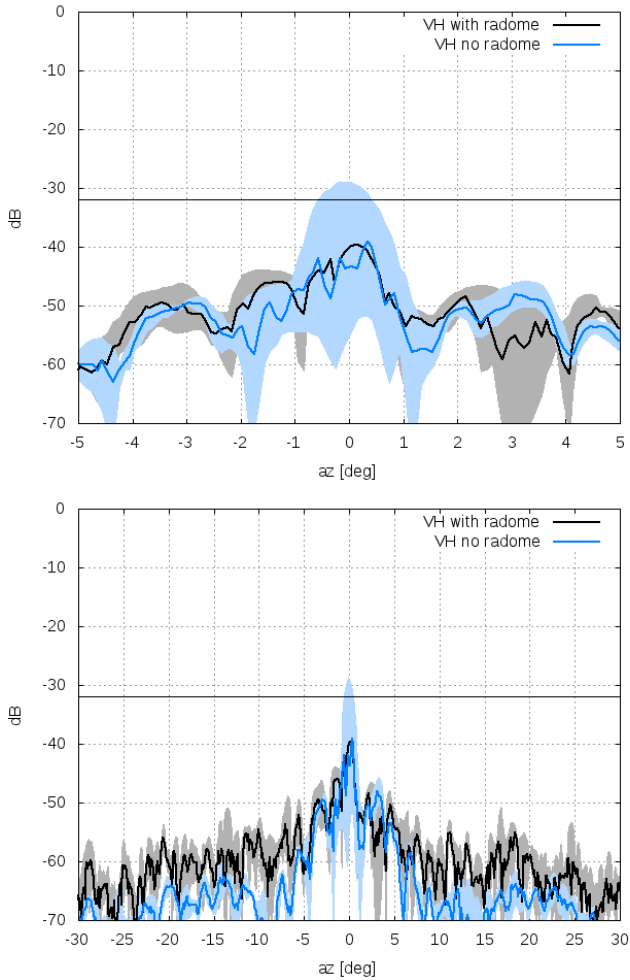


Figure 17: Variability of cross-polar power VH with and without radome in the main plane. Shown are also the antenna specifications.

the main plane, in particular for elevation angles $> 5^\circ$. Overall, the difference between the results with and without radome appear small in the strut plane. The blockage and scattering effects due to the struts dominate. The first side lobe in both cases is between -27 and -28 dB for both H and V. Up to 10° , the side lobes remain at an almost constant level of around -33 dB. There is no significant difference between measurements with and without radome. This has to be compared to the main plane results where we see a pronounced roll-off of the side lobe levels down to -50 dB or less for measurements without the radome, and -40 dB for measurements with the radome (see Figure 12). From radial angles $> 10^\circ$ on, we see a steady decrease in side-lobe levels. The specification are satisfied for angles of about $> 20^\circ$. The variability in the strut plane is shown in Figures 20 and 21. It is comparable for measurements with and without the radome. The cross-polar results in the strut plane are shown in Figure 19. A double peak at about $\pm 0.8^\circ$ can be seen where we cut through the typical cross-polar antenna pattern of a center fed antenna assembly (see also Figure 9). On average, the cross-polar levels in HV are within the specs whereas the peaks in VH are above the specification (near ≈ -28 dB). Similar to the variability of copolar cuts, the variability of cross-polar cuts through the strut plane is relatively small for both the measurements with and without radome (Figure 22 and 23). Clearly the copolar and cross-polar data in this plane is dominated by the presence of the struts.

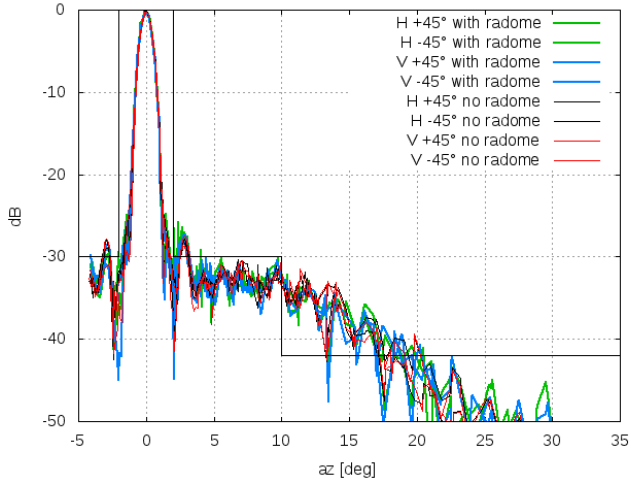


Figure 18: Average copolar power H and V, with and without radome. Shown are also the antenna specifications.

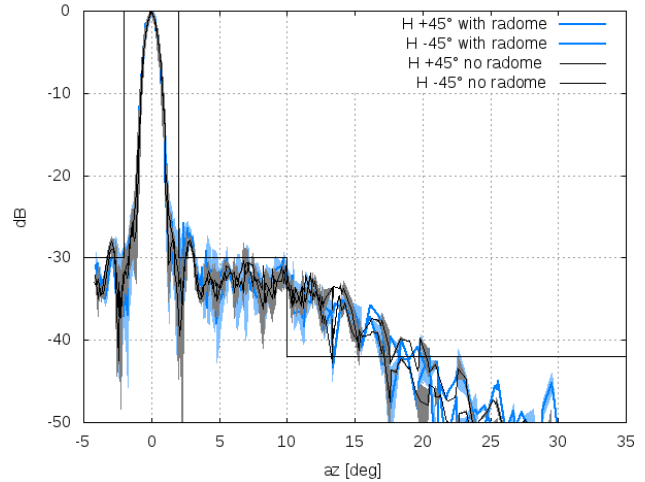


Figure 20: Variability of copolar power H with and without radome in the strut plane.

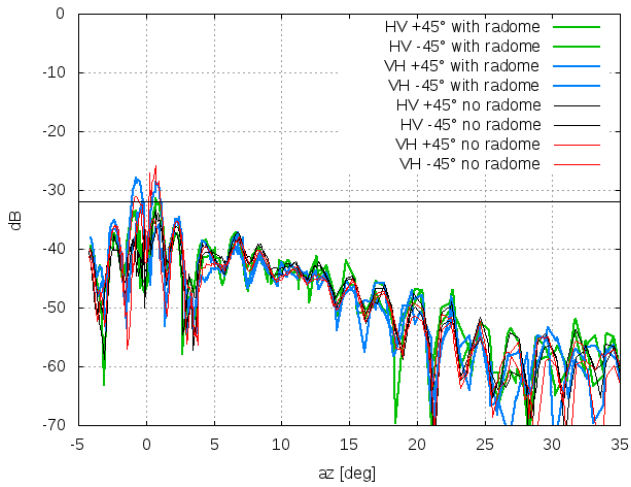


Figure 19: Average cross-polar power HV and VH, with and without radome. Shown are also the antenna specifications.

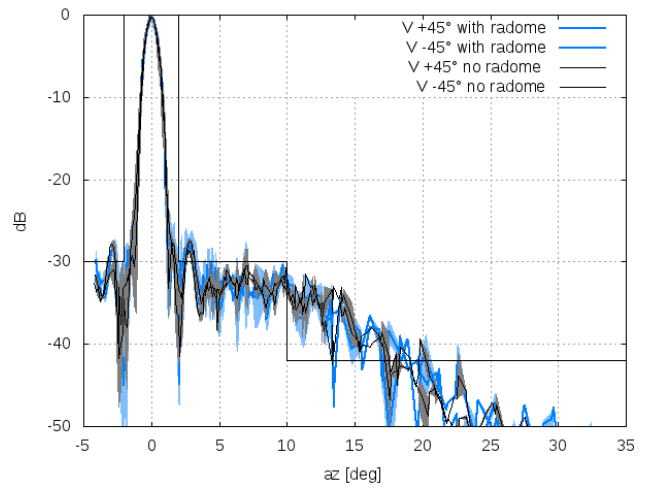


Figure 21: Variability of copolar power V with and without radome in the strut plane.

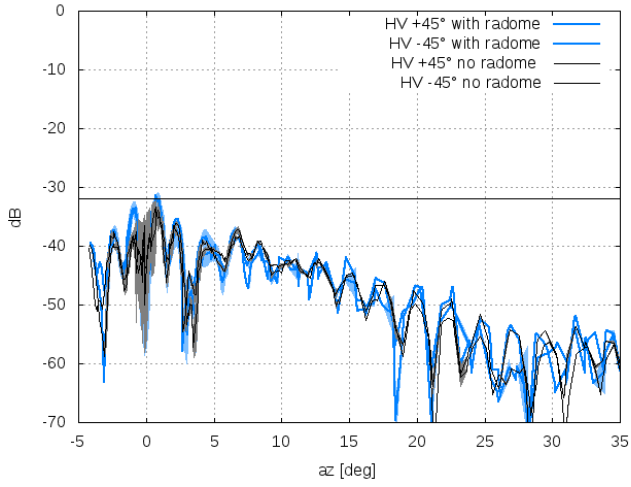


Figure 22: Variability of cross-polar power HV with and without radome in the strut plane.

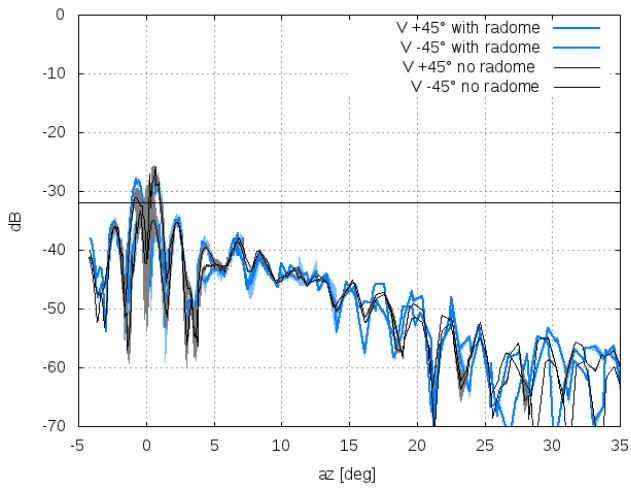


Figure 23: Variability of cross-polar power VH with and without radome in the strut plane.

8. Measurements of differential phase and differential power

In this section we focus on the match of the phase and power patterns.

A good match of the phase patterns is important to obtain good quality phase dependent radar moments, such as the differential phase Φ_{dp} and the cross correlation coefficient ρ_{hv} . Especially across the main beam, where most of the energy is located, variations of differential phase and power should be small. A variability of the differential measurements would limit the accuracy of radar moments under real weather conditions. However some variability might be expected due the presence of struts and errors in feed alignment (Mudukutore et al., 1995). As illustrating examples we show the spatial distribution of differential phase and power in the main beam areas for the measurements without radome (the figures with radome are comparable). The differential phase distribution is shown in Figure 24. The corresponding differential power measurement is shown in Figure 25. In the main beam area, the observed patterns for measurements with and without radome show similar pattern. Larger differences are found roughly at the border of the main beam. These differences will be quantified in the following. Large differences outside the main beam area related to usually low SNR values.

For a more detailed analysis we compute the phase difference as function of radial distance. The center or zero radial distance is defined as the location of the SNR peak power. For a given radial distance interval we compute the statistics of the data from all angles. This is done individually for all data with and without radome. The results based on the three source sites are then averaged to obtain the overall distribution of the phase difference in the main beam area. For the differential phase the results are shown in Figure 26. Up to about a radial distance of 1° , variations of differential phase are small for the measurements without radome. At about 1° we find a mean difference of -2° relative to the peak value in the main beam center. This corresponds to SNR values of about -15 dB below the main peak. Differences start to increase from about $r = 0.7^\circ$ on which also coincides with increased variability as seen in the 1st and 3rd quartile values. (Figure 26, lower panel). Up to

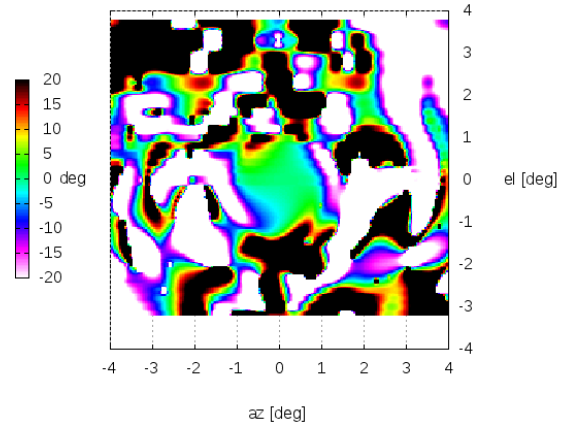


Figure 24: Differential phase without the radome. Source site is the TV tower.

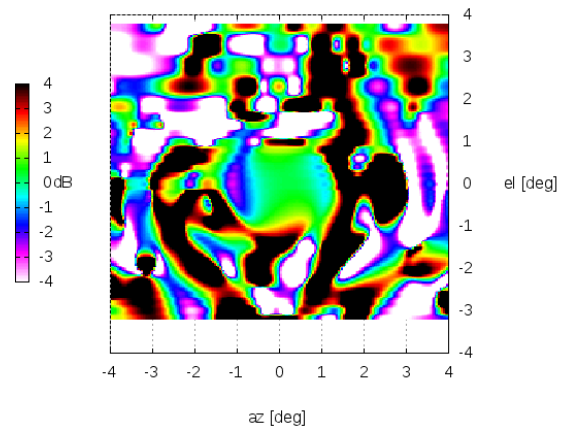


Figure 25: Differential power without the radome. Source site is the TV tower.

this value the phase difference is quasi-constant over the main beam. The measurements with radome on average show a somewhat larger increase in phase difference in the main beam area. Also the 1st and 3rd quartile appear to show a larger range suggesting an increased variability in differential phase due to the radome. The largest variability in differential phase is found around $r \approx 1.8^\circ$ where we find the first minimum in received copolar power (below -30 dB in SNRh).

The results for differential power are shown in Figure 27. On average, differential power is essentially 0 dB up to a radial distance of $r = 0.5^\circ$, which roughly corresponds to the 3dB beam width. This is found for the measurements with and without radome. With increasing radial distance r , the power difference increases up to ≈ 0.7 dB at $r = 1^\circ$. The increase is larger with radome where we reach a power difference of about ≈ 1 dB at $r = 1^\circ$. If the scattering volume is not beam-filling or heterogeneous, the observed differential power variability will affect the resulting data quality of ZDR (likely more than for the differential phase measurements).

9. Beam squint and beam width

Beam width and beam squint are important characteristics of an antenna. In the following we compute the beam width from the 3-D data by extracting the location of the -3 dB isoline relative to the peak of the main beam. We analyze data from the STAR and Single-Pol tests from three source sites. This is done separately for the tests with and without the new radome. In order to illustrate the differences in H and V, we show the H and V beam widths with and without radome on a one-to-one plot (Figure 28). First of all the beam widths are all below 1° . The results from the measurement with radome show a larger scatter (one outlier). Also, the data seem to suggest that the V beam widths are on average always larger than the H beam widths: without radome 0.90° (H) versus 0.93° (V), with radome 0.88° (H) versus 0.91° (V).

In order to compute the beam squint, we initially determine the position of the V peak relative to the main peak position in H. Then we fit a 2-D surface to the SNR data from which the peak positions in H and V are calculated. Those data are used to compute the beam squint. The errors in beams squint are determined by the un-

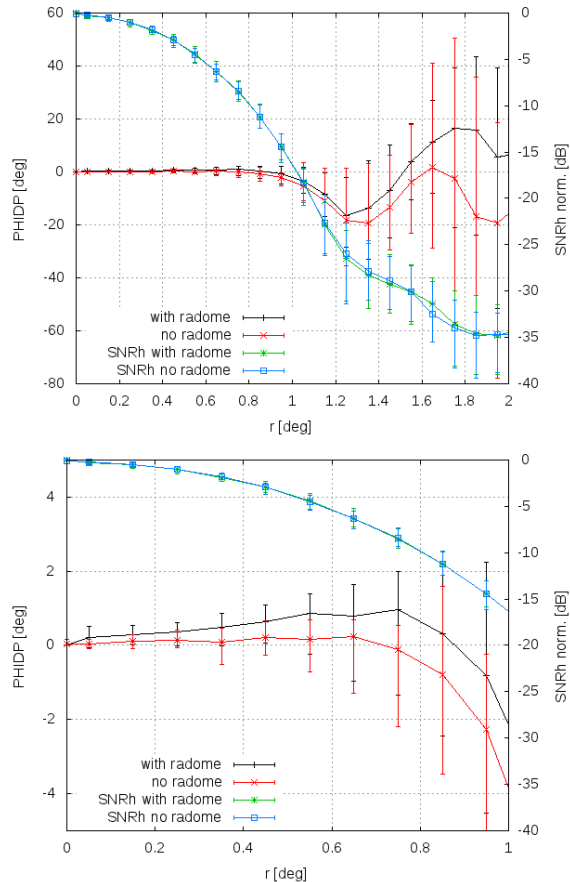


Figure 26: The differential phase without and with the radome as a function of radial distance relative to the main SNR peak. Shown are the median and the 1st and 3rd quartiles, respectively based on the pattern data from the three source sites. The upper panel shows the full range, whereas the lower panel shows a narrowed range in phase in order to see the differences in the main beam area.

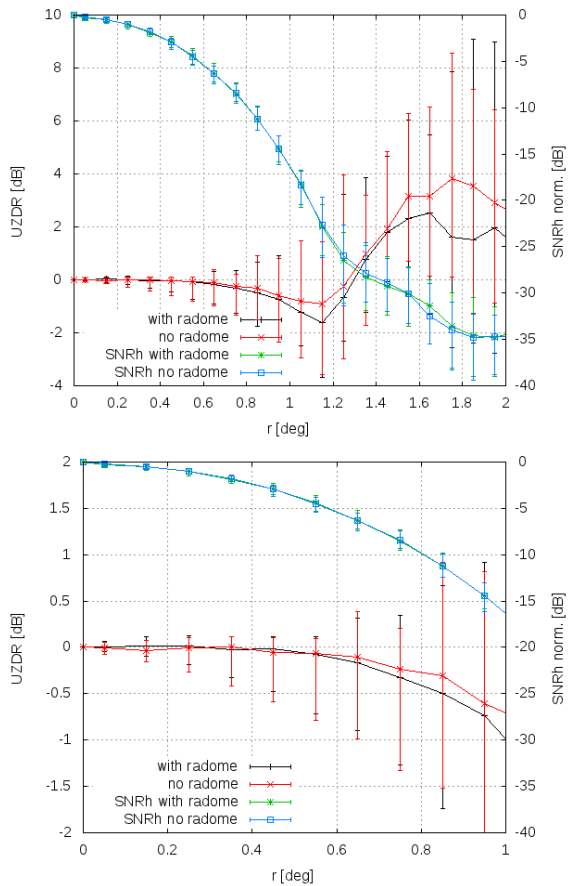


Figure 27: The differential power without and with the radome as a function of radial distance relative to the main SNR peak. Shown are the median and the 1st and 3rd quartiles, respectively based on the pattern data from the three source sites. The upper panel shows the full range, whereas the lower panel shows a narrowed range in differential power in order to see the differences in the main beam area.

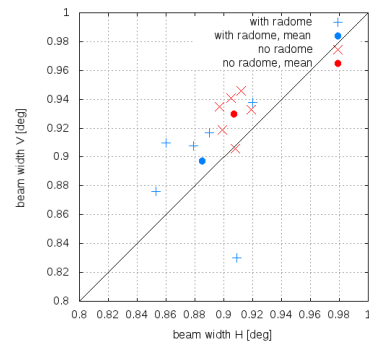


Figure 28: Beam widths in H and V, with and without radome.

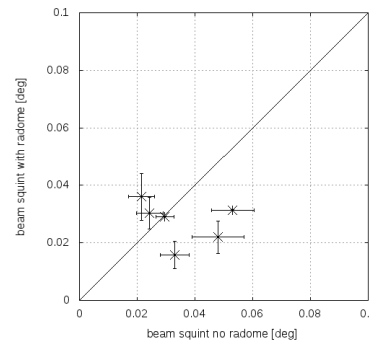


Figure 29: Beam squint with and without radome.

certainties of the surface fit. The results are shown in Figure 29. It should be noted that we the results actually represent the one-way beam squint. The beam squint with radome is always smaller than 0.04° , whereas two measurements without radome show a somewhat larger squint, but still below the specified 0.06° .

The results for beam width and squint are summarized in table 4.

Overall, the specification for beam width and squint are fulfilled with and without the radome.

Table 4: Beam widths (BW) and beam squint (BSQ) results with and without the radome and the differences in BW H and V. We show the average beam width in degrees.

| polarization | w/o radome | with radome |
|--------------|-----------------|-----------------|
| BW H | 0.91 ± 0.07 | 0.89 ± 0.07 |
| BW V | 0.93 ± 0.06 | 0.90 ± 0.05 |
| BW H-V | 0.023 | 0.012 |
| BSQ | 0.034 | 0.027 |

10. Conclusion

This unique measurement campaign is the first approach to quantify *on site* the performance and the effect of a radome on the HF performance of the antenna. Clearly, the specifications of the radome (in particular in the main beam area) and their proof are difficult to achieve, since the numbers are at or beyond the measurement accuracy of the radar system. Plus, there are always some uncertainties related to the test range conditions. Nevertheless, the statistics of the measurements indicate at least the magnitude of a radome effect, in particular if we compare the measurements with and without radome in the main plane directly. There, we have a very good data base to derive quantitative results. We find that the beam width, shape and squint do not degrade due to the radome. This in turn also means that the gain of the antenna should not degrade. The first side lobe level is raised in one polarization plane compared to measurements without radome. The side lobe levels are raised significantly off the main beam, but in general the resulting levels are on average still within the specifications. The STAR mode tests indicate that the inhomogeneity of differential phase in the main beam is larger due to the radome. The larger inhomogeneity appears related to different panel combinations seen by the antenna aperture considering the three source sites. This in turn implies some azimuthal dependence of the radar moments which still has to be quantified. The differential power measurements indicate a very good match up to the -3 dB level of the main beam. The power difference for the measurements with radome becomes larger with increasing radial distance (up to 1 dB). Here we may have

a larger ZDR bias due to the radome especially for situations with non-beam filling targets.

The data set is not yet fully analyzed. Ongoing analysis considers the antenna patterns which have to be quantitatively related to resulting moments. We also analyze weather cases in order to investigate antenna effects under strong spatial reflectivity gradients.

Acknowledgments: EEC is greatly acknowledged in supporting these comprehensive antenna measurements. Kay Desler, Thomas Hohmann, Ladislav Hart, Serguei Laskovitch and Manfred Feldman supported us significantly in achieving these measurements.

References

- Bringi, V. N., R. Hoferer, D. A. Brunkow, R. Schwerdtfeger, V. Chandrasekar, S. A. Rutledge, J. George, and P. C. Kennedy: 2011, Design and performance characteristics of the new 8.5m dual-offset Gregorian antenna for the CSU-CHILL radar. *J. Atmos. Ocean. Tech.*, **28**, 907–920.
- Chandrasekar, V. and R. J. Keeler: 1993, Antenna pattern analysis and measurements for multiparameter radars. *J. Atmos. Oceanic Tech.*, **10**, 674 – 683.
- Gourley, J. J., P. Tabary, and J. P. du Chatelet: 2006, Data quality of the Meteo-France C-Band Polarimetric Radar. *J. Atmos. Ocean. Tech.*, **23**, 1340–1356.
- Mudukutore, A., V. Chandrasekar, and E. A. Mueller: 1995, The differential phase pattern of the CSU CHILL radar antenna. *J. Atmos. Oceanic Tech.*, **12**, 1120 – 1123.
- Skolnik, M.: 2008, *RADAR handbook*. McGrawHill, 1328 pp.
- Zrnic, D., R. Doviak, G. Zhang, and A. Ryzhkov: 2010, Bias in differential reflectivity bias due to cross coupling through the radiation patterns of polarimetric weather radars. *J. Atmos. Ocean. Tech.*, **27**, 1624–1637.